

Water abundance in the lunar farside mantle

<https://doi.org/10.1038/s41586-025-08870-x>

Received: 10 September 2024

Accepted: 5 March 2025

Published online: 09 April 2025

Open access

 Check for updates

Huicun He^{1,5}, Linxi Li^{1,2,5}, Sen Hu¹✉, Yubing Gao^{1,2}, Liang Gao^{1,2}, Zhan Zhou^{1,2}, Mengfan Qiu^{1,2}, Disheng Zhou¹, Huanxin Liu¹, Ruiying Li¹, Jialong Hao¹, Hejiu Hui^{3,4,✉} & Yangting Lin¹✉

The water contents of the lunar interior record important clues for understanding the formation and subsequent thermochemical evolution of the Moon¹. The Chang'e-6 (CE6) mission returned samples from the South Pole–Aitken impact basin of the lunar farside^{2–4}, providing an opportunity to study the water contents of the farside mantle. Here we report the water abundances and hydrogen isotope compositions of apatite and melt inclusions from CE6 mare basalt, derived from partial melting of the lunar mantle. The parent magma of CE6 mare basalt is estimated to have a water abundance of 15–168 µg g⁻¹ with a δD value of $-123 \pm 167\text{‰}$. Our estimate of water abundance of 1–1.5 µg g⁻¹ for the mantle source indicates that the farside mantle is potentially drier than its nearside counterpart. This contrast thus suggests that the distribution of water in the interior of the Moon may exhibit a hemispheric dichotomy similar to numerous surface features⁵. The new estimate for the lunar farside mantle represents a landmark for estimating the water abundance of the bulk silicate Moon, providing critical constraints on the giant impact origin hypothesis^{6–8} and the subsequent evolution of the Moon for which the role of water is central^{1,9}.

Water abundance in the lunar mantle provides insights into the giant impact formation models for the Moon^{6–8} and plays a crucial role in the crystallization of the lunar magma ocean^{10,11} and subsequent magmatism and long-lived volcanism¹². In the past two decades, substantial advances in secondary ion mass spectrometry have improved our knowledge of water in the lunar mantle, causing a shift from the once traditional ‘bone dry’ concept¹³ to a relatively ‘wet’ Moon¹⁴. Extensive studies of various lunar samples derived from the melting of lunar mantle have shown a heterogeneous distribution of water in the lunar interior with abundances ranging from about 1 µg g⁻¹ to 200 µg g⁻¹ (refs. 9,15–19). However, most of these lunar water estimates derive from returned samples from the Procellarum KREEP Terrane on the nearside of the Moon (Fig. 1). The crust exposed at the surface of the Procellarum KREEP Terrane notably exhibits a higher thorium (Th) abundance than the other two main lunar geochemical provinces, the Feldspathic Highlands covering most of the Moon and the South Pole–Aitken (SPA) Basin, the oldest and largest impact basin of the Moon located on the lunar farside⁵.

Both Th and water behave like incompatible elements in magmatic processes, preferring to stay in the melt rather than getting incorporated in the solidifying phase, potentially suggesting that the lunar mantle in the Th-poor Feldspathic Highlands and the SPA Basin may have lower water content. This possibility, if true, could critically inform the spatiotemporal distribution of water in the mantle of the Moon, as well as the giant impact formation models^{6–8} and subsequent magmatic evolution histories of the Moon^{12,20}. However, little is known about the water abundance in the mantle beneath the Feldspathic Highlands and the SPA Basin. On 25 June 2024, Chang'e-6 (CE6), China’s lunar sample return mission landing within the SPA Basin, successfully returned the first lunar farside samples^{2–4}, providing the samples required to investigate the water abundance of the farside lunar mantle.

Water in CE6 apatite and melt inclusions

A total of 578 particles varying from 0.1–1.5 mm in size were sieved and hand-picked from one CE6 soil sample (CE6C0200YJFM001 of 5 g). Mare basalt fragments account for around 28% of the selected particles characterized by scanning electron microscopy and electron probe microanalysis (EPMA; Extended Data Table 1 and Supplementary Table 1). The mare basalts, derived from the partial melting of lunar mantle rocks, are the main targets selected for this study. The dominant hydrous mineral in mare basalts—apatite and entrapped melt hosted by olivine and ilmenite—were carefully characterized using scanning electron microscopy (Extended Data Fig. 1 and Supplementary Figs. 1–3) for further in situ chemical and isotopic analysis of water.

The studied CE6 mare basalt fragments display ophitic, subophitic, porphyritic and poikilitic textures, mainly composed of pyroxene, plagioclase, ilmenite and silica with minor olivine, mesostasis and sulfide and trace apatite (Supplementary Fig. 4), similar to a survey conducted with a large number of lithic clasts (Zhang, Q. W. L. et al., manuscript in preparation; Zhou, Q. et al., manuscript in preparation). Parallel studies conducted on the CE6 chronology (Zhang, Q. W. L. et al., manuscript in preparation) and petrogenesis (Zhou, Q. et al., manuscript in preparation) have shown that these low-Ti mare basalts probably derive from the same lava flow, or at least the same sequence of lava flows. Therefore, we sum up all the studied clasts to calculate the modal abundance of apatite (<0.07 vol%; Supplementary Table 2). Most melt inclusions hosted by olivine and ilmenite display post-entrapment crystallization of 31–52% (Extended Data Table 2). The chemical compositions of pyroxene and plagioclase in CE6 mare basalt fragments are similar to those from the nearside, such as those of Chang'e-5 (CE5; Extended Data Figs. 2 and 3). The apatite grains are F-rich, with compositions in the range of known mare basalts (Extended Data Fig. 4). Two CE6 mare

¹Key Laboratory of the Earth and Planetary Physics, Chinese Academy of Sciences, Beijing, China. ²College of Earth and Planetary Sciences, University of Chinese Academy of Sciences, Beijing, China. ³State Key Laboratory for Mineral Deposits Research and Lunar and Planetary Science Institute, School of the Earth Sciences and Engineering, Nanjing University, Nanjing, China. ⁴CAS Center for Excellence in Comparative Planetology, Hefei, China. ⁵These authors contributed equally: Huicun He, Linxi Li. ✉e-mail: husen@mail.igggcas.ac.cn; hhui@nju.edu.cn; linyt@mail.igggcas.ac.cn

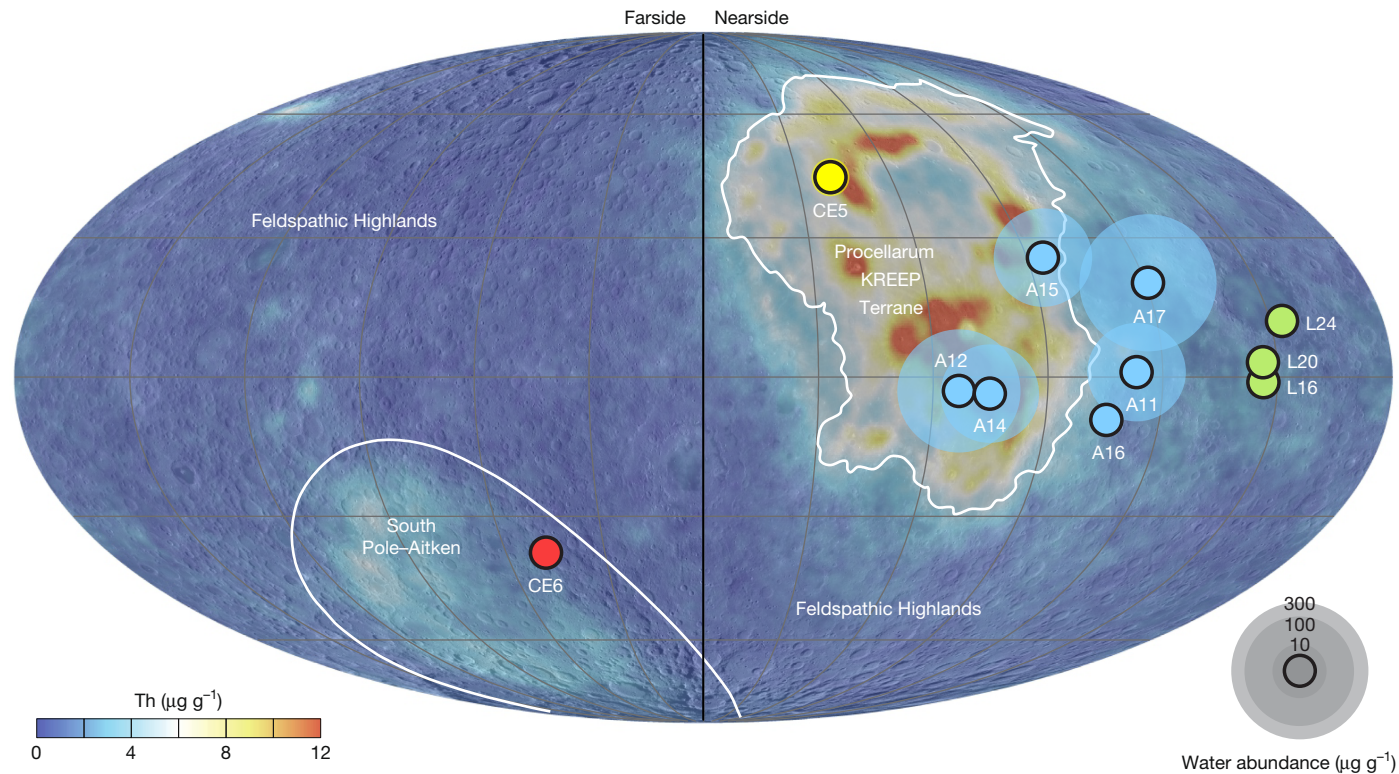


Fig. 1 | Return sample missions with lunar water estimates and the thorium distribution of the Moon. The Apollo (prefix A), Luna (prefix L), and Chang'e-5 (CE5) missions collected samples in and around the Procellarum KREEP Terrane which exhibits notably higher thorium (Th) than the Feldspathic Highlands and the SPA Basin. The Chang'e-6 (CE6) mission returned the

first lunar samples from the lunar farside from the SPA Basin. The terrane boundaries are from ref. 5 and the Th base map is adapted from ref. 45. The sizes of the circles are scaled to the estimated maximum water abundance^{1,9,33} in the mantle source beneath the sampling sites.

basalt fragments have MgO-rich olivine ($Fo = 45\text{--}62 \text{ mol}\%$) in which three melt inclusions were found (Extended Data Fig. 1, Supplementary Fig. 1 and Supplementary Table 3). Even more melt inclusions were found in ilmenite (Supplementary Fig. 2). Olivine-hosted melt inclusions have notably higher MgO (3.76–16.8 wt%) than ilmenite-hosted melt inclusions (<0.3 wt% MgO and 9.9–12.8 wt% Al_2O_3 ; Extended Data Fig. 5 and Supplementary Table 3). Tens of apatite grains with sizes of 5–30 μm and several melt inclusions hosted by olivine and ilmenite from 17 basalt fragments were also measured for their water abundance and hydrogen isotopic composition.

The CE6 basaltic apatite grains have water abundances ranging from $345 \pm 4 \mu\text{g g}^{-1}$ (2σ) to $3,529 \pm 30 \mu\text{g g}^{-1}$ (average $1,511 \pm 748 \mu\text{g g}^{-1}$, 1 s.d.) with δD ($\delta D = 1,000 \times ([D/\text{H}_{\text{sample}}]/[D/\text{H}_{\text{standard}}] - 1)$, using Vienna standard mean ocean water as the standard) values ranging from $657 \pm 72\text{\textperthousand}$ to $974 \pm 109\text{\textperthousand}$ (average $826 \pm 94\text{\textperthousand}$, 1 s.d.; Fig. 2 and Extended Data Table 3). The ilmenite-hosted melt inclusions contain water contents of $21 \pm 3 \mu\text{g g}^{-1}$ to $238 \pm 21 \mu\text{g g}^{-1}$ (2σ), with a wide range of δD values from $-183 \pm 261\text{\textperthousand}$ to about $1,000\text{\textperthousand}$ (Fig. 2 and Extended Data Table 2). By contrast, the olivine-hosted melt inclusions have water abundances ranging from $28 \pm 8 \mu\text{g g}^{-1}$ to $46 \pm 2 \mu\text{g g}^{-1}$ with δD values of $-358 \pm 610\text{\textperthousand}$ to $100 \pm 474\text{\textperthousand}$ (2σ ; Extended Data Table 2). All data were corrected for cosmic ray spallation using a cosmic ray exposure (CRE) age of 108 million years ago and those spots with H_2O less than twice the instrument background were excluded (Methods).

Water in parent melt and mantle source

Two methods were adopted to estimate water abundance in the parent melt of the CE6 basalts. The first method is based on apatite, which is the dominant water-bearing phase in lunar magmatic samples²¹.

The bulk rock of CE6 basalts is estimated to have a water abundance of $1.1 \pm 0.5 \mu\text{g g}^{-1}$ based on an average water abundance of $1,511 \pm 748 \mu\text{g g}^{-1}$ (1 s.d.; Extended Data Table 3) of apatite and a modal abundance of $\sim 0.07 \text{ vol\%}$ (Supplementary Table 2). By contrast, apatite grains in CE6 mare basalts show notably elevated δD values ($657 \pm 72\text{\textperthousand}$ to $974 \pm 109\text{\textperthousand}$; Extended Data Table 3) compared with the low δD (average at $-96 \pm 230\text{\textperthousand}$, 1 s.d.; Extended Data Table 3) of olivine-hosted melt inclusions and the recommended value of $-200 \pm 200\text{\textperthousand}$ for the lunar mantle^{22–24}. This difference indicates a notable loss of water by degassing in the form of H_2 before the crystallization of apatite under a reduced oxygen fugacity environment^{24,25}. This observation is consistent with the much lower hydrogen isotope compositions in mineral-hosted melt inclusions (Fig. 2). This feature is identical to that of high-Ti and low-Ti mare basalts collected from the nearside of the Moon (Fig. 2), suggesting that it resulted from a common degassing process incurred during mare volcanism. Thus, a degassing extent of $97.99\text{--}99.35\%$ based on Rayleigh fractionation (Methods) yields a water abundance of $55 \pm 25 \mu\text{g g}^{-1}$ to $168 \pm 77 \mu\text{g g}^{-1}$ (1 s.d.) for the parent melt of CE6 basalts, assuming an initial δD value of about $-200\text{\textperthousand}$ based on the analyses of D-poor and H_2O -rich CE6 melt inclusions hosted by olivine and ilmenite (Methods). Meanwhile, based on apatite–melt hygrometry^{1,26,27}, we estimated the parent magma to have a water abundance of $76 \pm 41 \mu\text{g g}^{-1}$ (Methods and Supplementary Table 6). Thus, both calculations on apatite yield comparable results within uncertainties.

The second method for estimating water in the parent melt uses the melt entrapped in minerals of CE6 basalts. Two types of mineral inclusions, hosted by olivine and ilmenite, were measured in this study (Fig. 2 and Extended Data Table 2). The analytical results for the melt inclusions depict an evolutionary pathway of the parent melt of the CE6 basalts, in which the entrapment of melts in olivine occurred in a

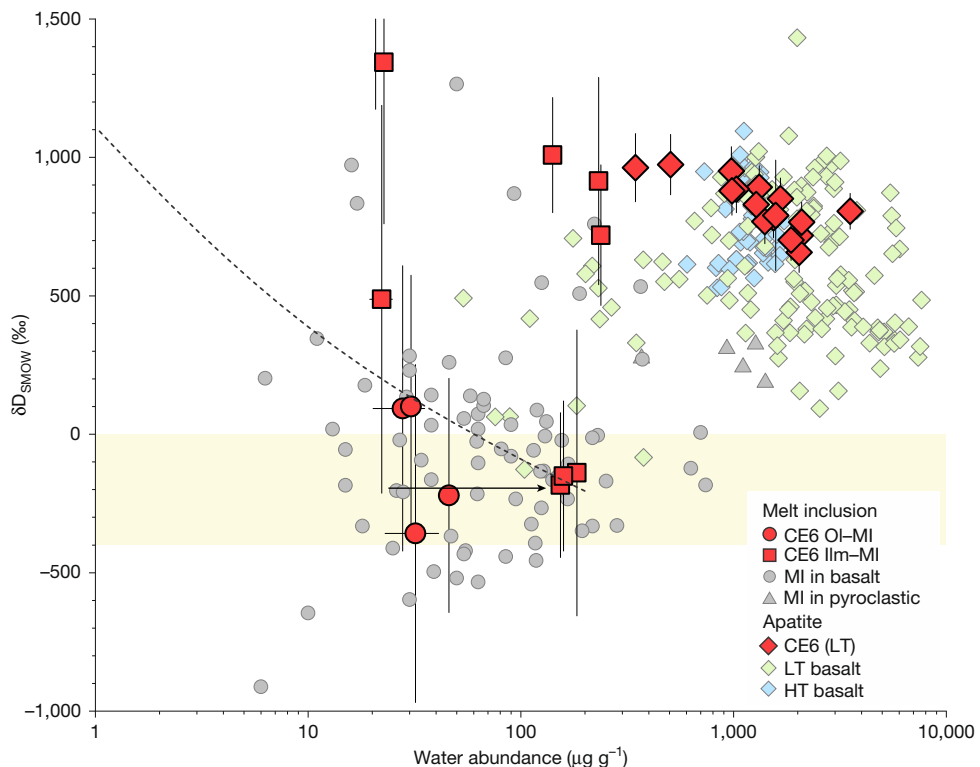


Fig. 2 | Water abundance and δD of melt inclusions and apatite from CE6 mare basalt fragments. Olivine-hosted melt inclusions have notably lower water abundances than ilmenite-hosted melt inclusions and apatite, as well as mostly lower δD values. Most melt inclusions have a lunar mantle-like δD value (yellow band)^{9,23,24,40}. Three ilmenite-hosted melt inclusions have elevated δD values that are unresolvable from those of apatite within analytical uncertainties. Melt inclusions from mare basalts (MI in basalt) are from refs. 9,23,42, high- and low-Ti mare basalts are referred to the datasets compiled by refs. 1,9. The CE6

datasets have been corrected for a nominal CRE of 108 million years (Methods). The arrow represents the enrichment of water in the residual melt during crystallization of the parent melt. The dashed line is the degassing trend from a water abundance of $200 \mu\text{g g}^{-1}$ with a δD value of $-200\text{\textperthousand}$. Note the horizontal axis is a log scale. The error bars are 2σ . OI-MI, olivine-hosted melt inclusion; ILM-MI, ilmenite-hosted melt inclusion; LT, low-titanium; and HT, high-titanium.

relatively earlier stage of magmatic processes than that of ilmenite, consistent with the crystallization sequence of other mare basalts²⁸ (Fig. 3). Olivine is the first-crystallized phase in the CE6 basalt and thus its melt inclusions may preserve the initial hydrogen isotope composition of the CE6 parental melt. Therefore, olivine-hosted melt inclusions are used to estimate the water abundance for the parent melt, yielding a range of $15\text{--}22 \mu\text{g g}^{-1}$ after correction for post-entrapment crystallization (Extended Data Table 2). These two methods yield a water abundance of about $15\text{--}168 \mu\text{g g}^{-1}$ for the CE6 basalt parent magma. This estimate is comparable to some values from some nearside samples (Extended Data Fig. 6).

The parent melt of CE6 mare basalts originated from the partial melting of a depleted mantle source, subsequently experienced fractional crystallization according to the study of its petrogenesis (Zhou, Q. et al., manuscript in preparation) and potential degassing during magmatic processes (Fig. 3). Early-formed melt inclusions hosted by olivine could be more reliable than the late-formed minerals and melt (Fig. 3). Thus, olivine-hosted melt inclusions were used to calculate the water abundance in the lunar farside mantle. Both Ce and H₂O exhibit similar incompatibilities, whereas Ce is not a volatile species²⁹, thus the resulting H₂O/Ce ratio of the parent melt can serve as a useful index to estimate water abundance for the mantle source^{1,30–32}. We calculated a H₂O/Ce ratio of 0.58–0.85 for the CE6 olivine-hosted melt inclusions using a bulk Ce abundance of $25.9 \mu\text{g g}^{-1}$ measured in Zhou, Q. et al. (manuscript in preparation). The mantle source of the CE6 mare basalt was estimated to have a water abundance of approximately $1\text{--}1.5 \mu\text{g g}^{-1}$ (Fig. 4 and Supplementary Table 7), considering a Ce content of $1.728 \mu\text{g g}^{-1}$ for the primitive lunar mantle³¹. This estimate

may represent an overestimate if considering the ultra-depleted nature for the mantle source of the CE6 mare basalt (Zhou, Q. et al., manuscript in preparation). The CE6 estimate represents the first result for the water abundance of the mantle from the farside of the Moon.

Distribution of lunar mantle water

A water abundance of $1\text{--}1.5 \mu\text{g g}^{-1}$ estimated for the mantle source of CE6 basalts plots among the lowest end of the ranges (about $1\text{--}200 \mu\text{g g}^{-1}$) reported from the nearside samples (Fig. 4), suggesting that the mantle source of CE6 mare basalt is drier than that of most nearside samples. A potential drier mantle in the farside of the Moon carries important implications for understanding the distribution of water in the interior of the Moon. This finding favours a heterogeneous distribution of water in the lunar mantle, consistent with the dichotomy distribution of Th concentration on the surface of the Moon⁵. If the whole farside mantle is similar to the mantle source of CE6 mare basalts and drier than the nearside counterpart, then the water abundance for the bulk silicate Moon may have been overestimated to some extent^{1,33}. Therefore, a lower water content in the bulk silicate Moon is expected, yielding a result more in line with the giant impact formation model of the Moon^{6–8}.

The dating of a large number of CE6 basalt clasts indicates that 99% of them belong to the local basalt erupted at about 2.8×10^9 years ago (Zhang, Q. W. L. et al., manuscript in preparation). The spatiotemporal evolution of water in the lunar mantle indicates that the water abundances may exhibit a spatial hemispheric contrast rather than a temporal trend based on the formation age of the samples (Fig. 4). A scenario to explain this lower water content is that the mantle source of CE6

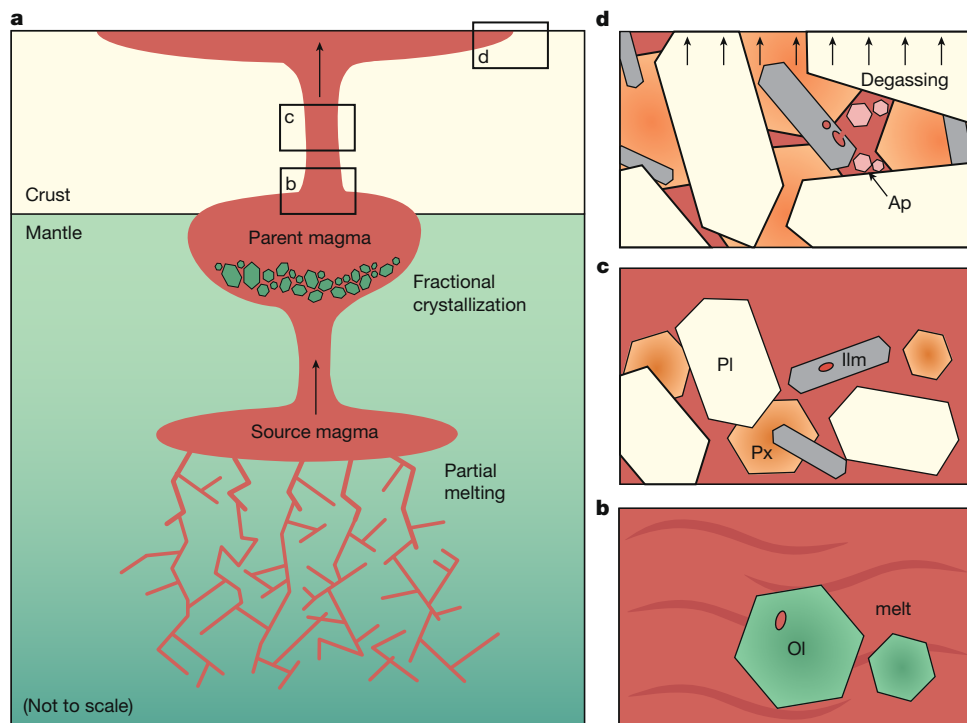


Fig. 3 | Evolutionary pathways of magmatic water in CE6 mare basalt. **a**, CE6 mare basalt was derived from the partial melting of lunar mantle rocks. The melt aggregates at depth in networks to form the source magma and intrudes upwards into shallow depths. The ambient rocks are much colder than the hot melt, resulting in fractional crystallization of the source magma. In certain circumstances, the residual melt (parent magma of CE6) from the source magma flowed up to the lunar surface, forming the rocks of CE6 mare basalt. The water abundances and hydrogen isotopic compositions measured on melt inclusions and apatite from the CE6 mare basalt depict an evolutionary pathway for water in the parent melt. **b**, Rare MgO-rich olivine (Fo 45–62 atom%; Supplementary Table 3) in CE6 mare basalt should crystallize much earlier than the main constituent phases (pyroxene and plagioclase) in the crystallization processes of the parent melt, characterized by a low water abundance and a

lunar-mantle-like δD value (Fig. 2) in the melt trapped in the olivine grains, as well as a notably high MgO content of the melt (Extended Data Table 2 and Extended Data Fig. 5, Supplementary Table 3). **c**, Onset of ilmenite formation in low-Ti mare basalts occurred at a late crystallization stage of the parent melt²⁸ accompanying enrichment of water in the residual melt followed by degassing of water when the ambient pressure is inadequate to trap the water dissolving in the melt. Thus, ilmenite-hosted melt inclusions exhibit variability in both water concentration and δD (Fig. 2). **d**, Apatite is one of the last-crystallized minerals in CE6 basalts, recording notable higher δD values than olivine-hosted melt inclusions. Some residual melt from which apatite crystallized may have been trapped by late-crystallized ilmenite (Fig. 2). Ol, olivine; Pl, plagioclase; Px, pyroxene; Ilm, ilmenite; and Ap, apatite.

basalts was affected to some extent by the SPA giant impact event, which may have driven the flux of water and other incompatible elements (Th, K and H₂O) enriched in the mantle of the Procellarum KREEP Terrane towards the lunar nearside and became simultaneously depleted in its hemispheric antipode in the SPA Basin^{34,35}. Another potential interpretation is a vertical distribution of water in the lunar mantle^{36,37}. The CE6 basalt originated from an extremely depleted mantle source, which may have a deeper depth of melting than most other lunar samples (Zhou, Q. et al., manuscript in preparation). Lunar mantle could have relatively less water for earlier and deeper crystallized cumulates than later and shallower cumulates formed from the lunar magma ocean because of the gradual enrichment of incompatible elements in the residual melt^{38,39}.

Origin of lunar mantle water

The analyses of olivine- and ilmenite-hosted melt inclusions consistently point to a parent melt of the CE6 basalts that had a δD value of $-123 \pm 167\text{‰}$ (1 s.d.; Methods). This value is indistinguishable from that ($-200 \pm 200\text{‰}$) derived from nearside samples^{9,23,24,40} within analytical uncertainties, suggesting that the mantle of the Moon could have a relatively homogeneous hydrogen isotopic composition, which does not show a spatiotemporal variation. This uniform hydrogen isotopic composition for the mantle source from various types and ages of

lunar samples in this study and previous works^{9,23,24,40} may have been inherited from the lunar magma ocean from which the mantle rocks crystallized⁴¹. Furthermore, the hydrogen isotopic composition of the farside mantle of the Moon favours a chondritic origin for the indigenous water of the Moon^{40,42}.

The first water estimate retrieved from the lunar farside indicates that water abundance in the lunar mantle may exhibit a hemispheric dichotomy (Fig. 4), similar to the well-known overlying crustal asymmetry of the nearside and the farside of the Moon⁵. Given the limited sampling of the lunar farside, it is still uncertain whether the potential drier mantle documented here is widespread beneath the SPA Basin or the whole farside hemisphere. New sample return missions scheduled by Artemis⁴³ and post-Chang'e programs⁴⁴ aim to collect more samples from the farside of the Moon, thus potentially testing and further unravelling the extremely heterogeneous distribution of the abundance of water on the Moon.

Online content

Any methods, additional references, Nature Portfolio reporting summaries, source data, extended data, supplementary information, acknowledgements, peer review information; details of author contributions and competing interests; and statements of data and code availability are available at <https://doi.org/10.1038/s41586-025-08870-x>.

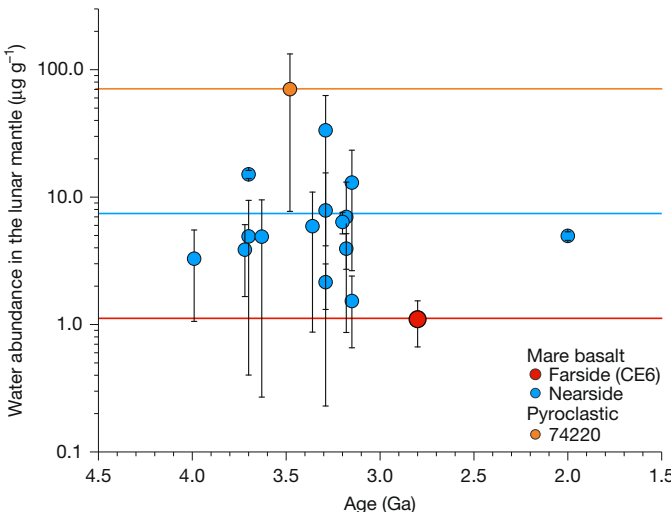


Fig. 4 | Spatiotemporal variation of lunar mantle water abundance estimates. The water abundance in the mantle source of CE6 mare basalt is estimated to be $1\text{--}1.5 \mu\text{g g}^{-1}$, plotting within the lowest end of the ranges from nearside samples. It is thus apparent that the lunar mantle may exhibit a hemispheric dichotomy in terms of water contents. The mantle water abundances estimated from Apollo and CE5 lunar samples with definite (non-ejecta) geographic locations are plotted for comparison^{9,33}. All data are plotted as average values with the error bars representing the ranges ($(\max - \min)/2$) of the estimates (Supplementary Table 7). The approximately 2.8 Ga age of the CE6 mare basalt is provided in Zhang, Q. W. L. et al. (manuscript in preparation). Note the vertical axis is the log scale. Red ($1.25 \mu\text{g g}^{-1}$), light blue ($7.5 \mu\text{g g}^{-1}$) and orange ($70.3 \mu\text{g g}^{-1}$) lines are the median H_2O abundances for the mantle sources estimated on the melt inclusions from the farside CE6 mare basalt, all nearside mare basalts and the nearside pyroclastic glasses.

- McCubbin, F. M. et al. Endogenous lunar volatiles. *Rev. Mineral. Geochem.* **89**, 729–786 (2023).
- Zeng, X. et al. Landing site of the Chang'e-6 lunar farside sample return mission from the Apollo basin. *Nat. Astron.* **7**, 1188–1197 (2023).
- Yue, Z. et al. Geological context of the Chang'e-6 landing area and implications for sample analysis. *Innovation* **5**, 100663 (2024).
- Li, C. et al. Nature of the lunar far-side samples returned by the Chang'e-6 mission. *Natl. Sci. Rev.* **11**, nwae328 (2024).
- Jolliff, B. L., Gillis, J. J., Haskin, L. A., Korotev, R. L. & Wieczorek, M. A. Major lunar crustal terranes: Surface expressions and crust-mantle origins. *J. Geophys. Res. Planets* **105**, 4197–4216 (2000).
- Canup, R. M. & Asphaug, E. Origin of the Moon in a giant impact near the end of the Earth's formation. *Nature* **412**, 708–712 (2001).
- Hartmann, W. K. & Davis, D. R. Satellite-sized planetesimals and lunar origin. *Icarus* **24**, 504–515 (1975).
- Lock, S. J. et al. The Origin of the Moon Within a Terrestrial Synestia. *J. Geophys. Res. Planets* **123**, 910–951 (2018).
- Hu, S. et al. A dry lunar mantle reservoir for young mare basalts of Chang'e-5. *Nature* **600**, 49–53 (2021).
- Lin, Y., Tronche, E. J., Steenstra, E. S. & van Westrenen, W. Evidence for an early wet Moon from experimental crystallization of the lunar magma ocean. *Nat. Geosci.* **10**, 14–18 (2017).
- Lin, Y., Tronche, E. J., Steenstra, E. S. & van Westrenen, W. Experimental constraints on the solidification of a nominally dry lunar magma ocean. *Earth Planet. Sci. Lett.* **471**, 104–116 (2017).
- Shearer, C. et al. Magmatic evolution II: a new view of post-differentiation magmatism. *Rev. Mineral. Geochem.* **89**, 147–206 (2023).
- Taylor, S. R., Pieters, C. M. & MacPherson, G. J. Earth-Moon system, planetary science, and lessons learned. *Rev. Mineral. Geochem.* **60**, 657–704 (2006).
- Saal, A. E. et al. Volatile content of lunar volcanic glasses and the presence of water in the Moon's interior. *Nature* **454**, 192–195 (2008).
- Boyce, J. W. et al. Lunar apatite with terrestrial volatile abundances. *Nature* **466**, 466–469 (2010).
- Greenwood, J. P. et al. Hydrogen isotope ratios in lunar rocks indicate delivery of cometary water to the Moon. *Nat. Geosci.* **4**, 79–82 (2011).
- Hauri, E. H., Weinreich, T., Saal, A. E., Rutherford, M. C. & Van Orman, J. A. High pre-eruptive water contents preserved in lunar melt inclusions. *Science* **333**, 213–215 (2011).

- Hui, H., Peslier, A. H., Zhang, Y. & Neal, C. R. Water in lunar anorthosites and evidence for a wet early Moon. *Nat. Geosci.* **6**, 177–180 (2013).
- McCubbin, F. M. et al. Nominally hydrous magmatism on the Moon. *Proc. Natl. Acad. Sci. USA* **107**, 11223–11228 (2010).
- Gaffney, A. M. et al. Magmatic evolution I: initial differentiation of the Moon. *Rev. Mineral. Geochem.* **89**, 103–145 (2023).
- McCubbin, F. M. & Jones, R. H. Extraterrestrial apatite: planetary geochemistry to astrobiology. *Elements* **11**, 183–188 (2015).
- Barnes, J. J. et al. An asteroidal origin for water in the Moon. *Nat. Commun.* **7**, 11684 (2016).
- Stephant, A. et al. The hydrogen isotopic composition of lunar melt inclusions: An interplay of complex magmatic and secondary processes. *Geochim. Cosmochim. Acta* **284**, 196–221 (2020).
- Tarté, R. & Anand, M. Late delivery of chondritic hydrogen into the lunar mantle: Insights from mare basalts. *Earth Planet. Sci. Lett.* **361**, 480–486 (2013).
- Sharp, Z. D., McCubbin, F. M. & Shearer, C. K. A hydrogen-based oxidation mechanism relevant to planetary formation. *Earth Planet. Sci. Lett.* **380**, 88–97 (2013).
- McCubbin, F. M., Lewis, J. A., Barnes, J. J., Elardo, S. M. & Boyce, J. W. The abundances of F, Cl, and H_2O in eucrites: Implications for the origin of volatile depletion in the asteroid 4 Vesta. *Geochim. Cosmochim. Acta* **314**, 270–293 (2021).
- McCubbin, F. M. et al. Experimental investigation of F, Cl, and OH partitioning between apatite and Fe-rich basaltic melt at 1.0–1.2 GPa and 950–1000 °C. *Am. Mineral.* **100**, 1790–1802 (2015).
- Li, L. et al. Petrogenesis of Chang'E-5 young mare low-Ti basalts. *Meteorit. Planet. Sci.* **58**, 1429–1448 (2023).
- Zhang, Y. X. H_2O and other volatiles in the Moon, 50 years and on. *ACS Earth Space Chem.* **4**, 1480–1499 (2020).
- Chen, Y. et al. Water, fluorine, and sulfur concentrations in the lunar mantle. *Earth Planet. Sci. Lett.* **427**, 37–46 (2015).
- Hauri, E. H., Saal, A. E., Rutherford, M. J. & Van Orman, J. A. Water in the Moon's interior: truth and consequences. *Earth Planet. Sci. Lett.* **409**, 252–264 (2015).
- Ni, P., Zhang, Y. X., Chen, S. & Gagnon, J. A melt inclusion study on volatile abundances in the lunar mantle. *Geochim. Cosmochim. Acta* **249**, 17–41 (2019).
- McCubbin, F. M. et al. Magmatic volatiles (H, C, N, F, S, Cl) in the lunar mantle, crust, and regolith: Abundances, distributions, processes, and reservoirs. *Am. Mineral.* **100**, 1668–1707 (2015).
- Jones, M. J. et al. A South Pole-Aitken impact origin of the lunar compositional asymmetry. *Sci. Adv.* **8**, eabm8475 (2022).
- Zhang, N. et al. Lunar compositional asymmetry explained by mantle overturn following the South Pole-Aitken impact. *Nat. Geosci.* **15**, 37–41 (2022).
- Anand, M., Tarté, R. & Barnes, J. J. Understanding the origin and evolution of water in the Moon through lunar sample studies. *Philos. Trans. R. Soc. A Math. Phys. Eng. Sci.* **372**, 20130254 (2014).
- Hauri, E. H. et al. Origin and evolution of water in the Moon's interior. *Annu. Rev. Earth Planet. Sci.* **45**, 89–111 (2017).
- Borg, L. E. & Carlson, R. W. The evolving chronology of Moon formation. *Annu. Rev. Earth Planet. Sci.* **51**, 25–52 (2023).
- Warren, P. H. The Magma ocean concept and lunar evolution. *Annu. Rev. Earth Planet. Sci.* **13**, 201–240 (1985).
- Barnes, J. J. et al. Early degassing of lunar urKREEP by crust-breaching impact(s). *Earth Planet. Sci. Lett.* **447**, 84–94 (2016).
- Hui, H. et al. A heterogeneous lunar interior for hydrogen isotopes as revealed by the lunar highlands samples. *Earth Planet. Sci. Lett.* **473**, 14–23 (2017).
- Saal, A. E., Hauri, E. H., Van Orman, J. A. & Rutherford, M. J. Hydrogen isotopes in lunar volcanic glasses and melt inclusions reveal a carbonaceous chondrite heritage. *Science* **340**, 1317–1320 (2013).
- Smith, M. et al. The Artemis Program: an overview of NASA's activities to return humans to the Moon. In Proc. 2020 IEEE Aerospace Conference 1–10 (IEEE, 2020).
- Xu, L., Li, H., Pei, Z., Zou, Y. & Wang, C. A brief introduction to the International Lunar Research Station program and the Interstellar Express mission. *Chin. J. Space Sci.* **42**, 511–513 (2022).
- Lawrence, D. J. et al. High resolution measurements of absolute thorium abundances on the lunar surface. *Geophys. Res. Lett.* **26**, 2681–2684 (1999).

Publisher's note Springer Nature remains neutral with regard to jurisdictional claims in published maps and institutional affiliations.



Open Access This article is licensed under a Creative Commons Attribution-NonCommercial-NoDerivatives 4.0 International License, which permits any non-commercial use, sharing, distribution and reproduction in any medium or format, as long as you give appropriate credit to the original author(s) and the source, provide a link to the Creative Commons licence, and indicate if you modified the licensed material. You do not have permission under this licence to share adapted material derived from this article or parts of it. The images or other third party material in this article are included in the article's Creative Commons licence, unless indicated otherwise in a credit line to the material. If material is not included in the article's Creative Commons licence and your intended use is not permitted by statutory regulation or exceeds the permitted use, you will need to obtain permission directly from the copyright holder. To view a copy of this licence, visit <http://creativecommons.org/licenses/by-nc-nd/4.0/>.

© The Author(s) 2025

Methods

Sample preparation

Five grams of scooped Chang'e-6 (CE6) lunar soil (CE6C0200YJFM001) allocated by the China National Space Administration (CNSA) were used in this study. The allocated samples were sieved into two dividers in an ultraclean room at the Institute of Geology and Geophysics, Chinese Academy of Sciences (IGGCAS) in Beijing, China. One separate was $>355\text{ }\mu\text{m}$ and the other was $<355\text{ }\mu\text{m}$. Eighty-eight particles $>355\text{ }\mu\text{m}$ were selected and prepared into 7 Sn–Bi polished mounts following the protocol in ref. 46. The mounts were labelled as CE6C02,MGP01–MGP07 (Extended Data Table 1 and Supplementary Table 1). Another 490 particles with grain sizes ranging from $100\text{ }\mu\text{m}$ to $350\text{ }\mu\text{m}$ were hand-picked from the sieved soils. These particles were placed in a tunnel (depth about $300\text{ }\mu\text{m}$, width about $400\text{ }\mu\text{m}$ and length about 1.8 mm) of silica glass cut by low-speed diamond saw (Supplementary Fig. 5). Then the tunnel was filled up with epoxy. These particles were finally prepared into 14 polished thick sections labelled as CE6C02,WGP01–WGP14 (Extended Data Table 1 and Supplementary Table 1). The prepared sections were cleaned up using anhydrous ethanol before drying at $50\text{ }^{\circ}\text{C}$ in a baking oven. All the mounts were coated with carbon for petrographic observation, chemical analysis and isotopic analysis. Statistically, the particles used in this study consist of 163 mare basalt fragments (28%), 97 monomineralic fragments (17%), 50 agglutinates (9%), 101 breccias (18%), 52 highlands fragments (9%), 76 impact melt fragments (13%) and 39 glass beads and fragments (7%) (Extended Data Table 1). Representative petrography of these components in the CE6 lunar soils is shown in Supplementary Fig. 6.

Scanning electron microscopy

Petrographic observations and elemental mapping were carried out using field emission scanning electron microscopes using the FEI Nova NanoSEM 450 and the Thermo Fisher Apreo instruments at IGGCAS, using electron beam currents of 2–3.2 nA and an acceleration voltage of 15 kV. Energy dispersive spectroscopy (EDS) X-ray maps were collected for each basaltic clast to locate P-bearing phases, identical to the protocol used in the study of CE5 lunar soils^{9,47,48}. The phosphates were then observed at higher magnification in back-scattered electron (BSE) images. The modal abundance of apatite from various CE6 basalt fragments was counted by the exposed surface areas (Supplementary Table 2). The apatite in the studied samples has a modal abundance of 0.067 vol% calculated from 163 basalt fragments using ImageJ software (Supplementary Table 2 and Supplementary Fig. 7).

Electron probe microanalysis

The major and minor elemental abundances in phosphates, glassy melt inclusions and associated minerals (olivine, pyroxene, plagioclase and ilmenite) were measured using a JEOL JXA-8100 electron probe microanalyser at IGGCAS after the NanoSIMS measurements to avoid possible H loss due to bombardment by the electron beam⁴⁹. For silicate, ilmenite and apatite analysis, the operating accelerating voltage was 15 kV and the beam current was 20 nA. The standards used were albite for Na and Al, diopside for Si, Mg and Ca, magnetite for Fe, bustamite for Mn, sanidine for K, rutile for Ti, Cr_2O_3 for Cr, NiO for Ni, apatite for P, tugtupite for Cl and synthetic fluorite for F. The F K α X-rays were counted with a LDE1 crystal to avoid drift with time (ref. 50). F and Cl were measured first to minimize the loss of volatiles by electron beam irradiation. The counting time for F was 20 s. The detection limits (1σ) were 0.01 wt% for K_2O , P, F, and Cl; 0.02 wt% for Cr_2O_3 , Al_2O_3 , MnO , CaO , FeO , TiO_2 and NiO; 0.03 wt% for SiO_2 and Na_2O . For analysis of melt inclusion glass, the accelerating voltage was 15 kV and the beam current was 10 nA, with a beam size of $5\text{ }\mu\text{m}$ in diameter to obtain the composition of the glass within a melt inclusion. A natural obsidian glass was used as a monitor. The detection limits for MI were 0.02 wt% for K_2O , CaO , FeO and NiO; 0.03 wt% for SiO_2 , MgO , Cr_2O_3 , Al_2O_3 , MnO and TiO_2 ; and

0.04 wt% for Na_2O . The EPMA data obtained for apatite, melt inclusions and the coexisting silicates are listed in Supplementary Table 3.

In situ water abundance and hydrogen isotope analysis

A CAMECA NanoSIMS 50L at IGGCAS was used to measure the hydrogen isotopes and water abundance of apatite and melt inclusions from the CE6 basaltic fragments. The samples were loaded in sample holders together with the standards, and were baked overnight at about $60\text{ }^{\circ}\text{C}$ in the airlock chamber. The holders were then stored in the NanoSIMS vessel chamber to improve the vacuum quality and minimize the H background^{51,52}. The vacuum pressure in the analysis chamber was 2.1×10^{-10} torr to 3.0×10^{-10} torr during analysis facilitated by a liquid nitrogen cold trap⁵³. Each $15\text{ }\mu\text{m} \times 15\text{ }\mu\text{m}$ analysis area was pre-sputtered for 2 min with a Cs^+ ion beam current of 5 nA to remove the surface coating and potential contamination. A $4\text{ }\mu\text{m} \times 4\text{ }\mu\text{m}$ region of interest on targets was selected for analysis. The secondary anions ${}^1\text{H}^-$, ${}^2\text{D}^-$, ${}^{12}\text{C}^-$ and ${}^{18}\text{O}^-$ were simultaneously counted by electron multipliers from the central $3\text{ }\mu\text{m} \times 3\text{ }\mu\text{m}$ areas using the electronic gate technique of NanoSIMS (about 50% blanking). The ion beam current (Fco) was around 0.5 nA for analysis with a beam size of about 500 nm in diameter. The charging effect on the surface of the samples was compensated by an electron gun during analysis. More details are provided in refs. 52,54.

A series of apatite and glass standards were used for calibrating the water abundances and hydrogen isotopes of the samples: Durango apatite ($\text{H}_2\text{O} = 0.0478\text{ wt\%}$ and $\delta\text{D} = -120 \pm 5\text{\%}$) (refs. 16,55) and Kovdor apatite ($\text{H}_2\text{O} = 0.98 \pm 0.07\text{ wt\%}$ and $\delta\text{D} = -66 \pm 21\text{\%}$) (ref. 56), the SWIFT MORB glass ($\text{H}_2\text{O} = 0.258\text{ wt\%}$ and $\delta\text{D} = -73 \pm 2\text{\%}$), and two basaltic glasses, ALV-519-4-1 ($\text{H}_2\text{O} = 0.17\text{ wt\%}$) (ref. 51) and ALV-1833-11 ($\text{H}_2\text{O} = 1.2\text{ wt\%}$) (ref. 51) (Supplementary Table 4). The water content calibration lines established on apatite and glass standards were used for calibrating the samples (Extended Data Fig. 7). Instrument mass fractionation (IMF) on hydrogen isotopic composition are the same between apatite and silicate glass within analytical uncertainties (Extended Data Fig. 7). Instrumental mass fractionation on H isotopic compositions of both apatite and melt inclusions were conducted using the Kovdor apatite standard and monitored by analysing both the Durango apatite and SWIFT MORB glass standards during the whole analytical session (Extended Data Fig. 7). Hydrogen isotopic compositions are given using the delta notation, $\delta\text{D} = ((\text{D}/\text{H})_{\text{sample}}/(\text{D}/\text{H})_{\text{SMOW}} - 1) \times 1,000\text{\%}$, where SMOW is the standard mean ocean water with a D/H ratio of 1.5576×10^{-4} (ref. 57).

The instrument H background was monitored by standards of San Carlos olivine⁵⁸ ($\text{H}_2\text{O} = 1.4\text{ }\mu\text{g g}^{-1}$) and a synthetic anhydrous quartz glass Suprasil 3001 (personal communication with Erik Hauri). The H background correction of ref. 59 was used, which follows the relationship: $\text{H}/\text{O}_{\text{bg}} = (\text{H}_{\text{counts}} - \text{H}_{\text{bg}})/\text{O}_{\text{counts}}$ and $\text{D}/\text{H}_{\text{measured}} = (1 - f) \times \text{D}/\text{H}_{\text{true}} + f \times \text{D}/\text{H}_{\text{bg}}$, where f is the proportion of H emitted from the instrumental background. Owing to the inadequate baking and storing time in the instrument, the first 2 days have a slightly higher instrument background at $26\text{--}53\text{ }\mu\text{g g}^{-1}$ ($\text{D}/\text{H}_{\text{bg}}$ was $(1.40 \pm 0.25) \times 10^{-4}$ to $(1.13 \pm 0.41) \times 10^{-4}$ and H_{bg} was 1546 ± 266 counts per second (cps) to 786 ± 81 cps (Supplementary Table 4)). The instrument H_2O background was about $10\text{ }\mu\text{g g}^{-1}$ ($\text{D}/\text{H}_{\text{bg}}$ was $(1.19 \pm 0.26) \times 10^{-4}$ to $(1.14 \pm 0.49) \times 10^{-4}$ and H_{bg} was 374 ± 170 cps to 311 ± 37 cps) in the following days (Supplementary Table 4)). After background subtraction, the water abundances of apatite and melt inclusions were quantified by the slope of the calibration line (Extended Data Fig. 7), which was determined by measuring apatite and glass standards.

All data are reported with their 2σ uncertainties that include reproducibility of D/H measurements on the reference materials, uncertainty of H_2O background subtraction, internal precision on each analysis and uncertainty of corrections of spallation effects (Supplementary Table 5). The raw measured D/H ratios were corrected for the background, followed by IMF and spallation in sequence (Supplementary Table 5).

Correction of water abundances and D/H ratios for spallation effects

The measured D/H ratios have been corrected for the potential effects of spallation by CRE, using a D production rate of 2.17×10^{-12} mol D/g/Ma (ref. 60) for melt inclusions and 9.20×10^{-13} mol D/g/Ma (ref. 61) for apatite, where Ma signifies millions of years ago. The correction errors induced by D spallation are around 50% for δD and negligible for water content⁴². The CRE age for the CE6 lunar soils derives from a cosmogenic ^{21}Ne age of 146 ± 27 Ma (T_{21} ; Zhang, X. et al., manuscript in preparation), which was converted to an exposure age (T_{CRE}) of 108 ± 20 Ma using an empirical relationship ($T_{21} = 1.35 \times T_{\text{CRE}}$) between T_{21} and T_{CRE} based on the study of Apollo samples⁶⁰. An uncertainty of 50% (2σ) in D and H production rates raised by the spallation process was combined to calculate its contribution to the δD errors (ref. 42; Supplementary Table 5).

Petrography of CE6 mare basalt

Approximately 28% of the lithic clasts in a total of 578 fragments studied in this work are mare basalt fragments (Supplementary Table 1), which display subophitic, poikilitic and porphyritic textures (Supplementary Fig. 4), similar to those in Zhang, Q. W. L. et al. (manuscript in preparation) and Zhou, Q. et al. (manuscript in preparation). Lath-shaped plagioclase in the basalts exhibits sharp boundaries, whereas pyroxene is anhedral with compositional zonation in BSE images (Supplementary Fig. 4). These basalt fragments are mainly composed of pyroxene, plagioclase and ilmenite with minor Si-K-rich mesostasis, fayalite and troilite, and trace apatite, merrillite, tranquillityite and baddeleyite (Supplementary Fig. 4). Olivine is very rare and absent in most CE6 mare basalt except two basalt fragments (CE6C02,WGP09,G17 and CE6C02,WGP14,G3), as shown in this study and other parallel studies (Zhang, Q. W. L. et al., manuscript in preparation; Zhou, Q. et al., manuscript in preparation). These two olivine grains have several melt inclusions with diameters of about 5–50 μm (Extended Data Fig. 1 and Supplementary Fig. 1). Melt inclusions have experienced post-entrainment crystallization (31–52%) (Extended Data Fig. 1, Extended Data Table 2 and Supplementary Fig. 1). Ilmenite intergrows with plagioclase but has a smaller size and irregular edge, occurring as laths partially enclosed by pyroxene (Supplementary Fig. 1). Nine melt inclusions in ilmenite were identified in 7 CE6 mare basalt fragments with diameters mostly less than 30 μm (Supplementary Fig. 2). Ilmenite-hosted melt inclusions have experienced post-entrainment crystallization (0–31%) (Extended Data Table 2 and Supplementary Fig. 2). Phosphorus- and zirconium-bearing minerals mainly occur in the fine-grained interstitial areas. Several apatite grains are observable in the margins of plagioclase and pyroxene (Supplementary Fig. 3). Most apatite grains have euhedral shape and rare ones are lath-shaped (Supplementary Fig. 3). CE6 mare basalts have notably less apatite (0.067 vol%; Supplementary Table 2) than CES basalts (0.4 vol%) (ref. 9). Meanwhile, apatite grains in CE6 mare basalt fragments have smaller sizes (mostly <5 μm; Supplementary Fig. 3).

Mineral chemistry of CE6 mare basalt

Plagioclase from CE6 basalt clasts is relatively homogeneous with a composition of $\text{An}_{75.2-92.5}\text{Ab}_{5.3-20.1}\text{Or}_{0.1-5.0}$ (Extended Data Fig. 3 and Supplementary Table 3). The pyroxene displays compositional zonation from Mg-rich cores ($\text{En}_{42.1-56.1}\text{Wo}_{9.1-38.1}\text{Fs}_{20.7-49.5}$) to Fe-rich rims ($\text{En}_{0.3-25.9}\text{Wo}_{11.6-47.3}\text{Fs}_{47.8-87.6}$) (Extended Data Fig. 2 and Supplementary Table 3). Ilmenite shows no chemical difference between various basalt fragments, containing about 52.9 wt% TiO_2 and about 46.2 wt% FeO, with minor other elements (Supplementary Table 3). Most CE6 basalt fragments contain trace fayalite ($\text{Mg}^{\#} < 1$). Two relatively large olivine grains having melt inclusions identified in this study are quite homogeneous in chemistry with average $\text{Mg}^{\#}$ of 49.3 ± 2.7 and 59.1 ± 2.2 (σ , $n = 5$; Extended Data Fig. 3 and Supplementary Table 3). Interstitial mesostasis is SiO_2 -rich (65.2–76.9 wt%) and K_2O -rich (2.40–7.65 wt%;

Supplementary Table 3). Olivine- and ilmenite-hosted melt inclusions have 38.0–79.9 wt% SiO_2 , 0.61–7.13 wt% TiO_2 , 5.43–17.5 wt% Al_2O_3 , 0.68–15.6 wt% CaO and 1.44–33.1 wt% FeO (Extended Data Fig. 5 and Extended Data Table 3). Concentrations of MgO in olivine-hosted melt inclusions range from 3.76 wt% to 16.8 wt%, whereas those of melt inclusions in ilmenite are less than 0.30 wt%. Melt inclusions in olivine have lower SiO_2 contents (38.0–60.6 wt%) compared with ilmenite-hosted ones (44.5–79.9 wt%), indicating an earlier entrapment for the former. Apatite grains in this study contain 2.54–4.08 wt% F and 0.09–0.43 wt% Cl (Supplementary Table 3), close to the fluorapatite end-member in the F–Cl–OH ternary diagram (Extended Data Fig. 4). The evaluated OH contents of apatite range from 0 wt% to 0.22 wt%, assuming the volatile site only contains F, Cl and OH. Apatite grains in CE6 mare basalt fragments are usually less than 5 μm, rendering it unavoidable to sample some surrounding minerals during EPMA and yielding an EPMA total usually less than 98 wt% (Supplementary Table 3).

Estimate of water abundance for the parent melt of CE6 mare basalt

Melt inclusions. Melt inclusions are trapped melt in the minerals during crystallization of the parent melt. Three melt inclusions were identified in olivine from two CE6 mare basalt fragments (CE6C02,WGP09,G17 and CE6C02,WGP14,G3; Extended Data Table 2 and Supplementary Fig. 1). These olivine-hosted melt inclusions have a water abundance of 28–46 $\mu\text{g g}^{-1}$, slightly higher than the instrument background, with large variation in δD values ($-358 \pm 610\%$ to $100 \pm 474\%$) after correction of spallation effects (Extended Data Table 2). The correction of spallation can markedly affect δD for those samples with water abundances <50 $\mu\text{g g}^{-1}$ (ref. 42). The hydrogen isotopic compositions for analyses with $\text{H}_2\text{O} < 20 \mu\text{g g}^{-1}$ may not be reliable because of the extremely low measured D counts¹. Thus, those spots with $\text{H}_2\text{O} < 20 \mu\text{g g}^{-1}$ (that is, two times the instrument background) are not discussed or used in deriving the water abundance for the parent magma and for the mantle source (Extended Data Table 2). An average δD of $-96 \pm 230\%$ (1 s.d.) in olivine-hosted MIs is comparable to some early trapped melt hosted by ilmenite, which have water abundances of 153–184 $\mu\text{g g}^{-1}$ and δD values of -183% to -140% with an average value of $-158 \pm 23\%$ (1 s.d.; Fig. 2 and Extended Data Table 2). The low-δD nature of the melt inclusions hosted by olivine and by early-formed ilmenite are comparable to the mantle δD value ($-200 \pm 200\%$) recommended in previous studies^{9,23,40,62}, indicating that these MIs plausibly represent the parent melt in the terms of water abundance and hydrogen isotope signature. This prediction is also supported by the high MgO content in olivine-hosted melt inclusions compared with previous work^{23,30,32}.

The host olivine grains of melt inclusions have forsterite content of 45.0–61.6 atom% (Supplementary Table 3), indicative of early precipitation phases crystallized from the parent melt of the CE6 mare basalt. In comparison, CE6 mare basalt has a slightly lower bulk Ti abundance (4.2 wt%) (Zhou, Q. et al., manuscript in preparation) than that of CES (5.3 wt%) (ref. 63), which would result in the late precipitation of ilmenite from the parent melt as shown by modelling²⁸. A gap in water abundance between olivine- and ilmenite-hosted melt inclusions could be the result of the crystallization sequence (Fig. 2). It is also noted that some ilmenite-hosted melt inclusions have comparable values to apatite, suggesting a late entrainment probably accompanying the onset of apatite at a quite late crystallization stage. Therefore, we provide an illustration diagram depicting the potential evolutionary pathways of magmatic water for CE6 mare basalt (Fig. 3). Finally, the δD-poor spots of olivine-hosted melt inclusions are regarded as a target for estimating the water abundance of the parent melt. We estimate a water abundance of 15–22 $\mu\text{g g}^{-1}$ for the parent melt of the CE6 mare basalt based on the olivine-hosted melt inclusions (Extended Data Table 2). Excluding the notable high δD ilmenite-hosted melt inclusions probably formed accompanying apatite in the late crystallization stages, we estimate the

Article

parent melt of the CE6 mare basalt as having a δD value of $-123 \pm 167\%$ (1 s.d.) (Extended Data Table 2).

Apatite. Apatite is the major OH-bearing phase in lunar igneous rocks¹. A modal abundance and an average water abundance of apatite were used to quantify water in bulk CE6 basalts. Statistically assessed using the surface areas of apatite grains in all basaltic clast, the modal abundance of apatite in CE6 basalts is found to be less than 0.07 vol% (Supplementary Table 2). The average water content and δD value of the CE6 apatite measured by NanoSIMS 50L are $1,511 \pm 748 \mu\text{g g}^{-1}$ and $826 \pm 94\%$ (1 s.d., $n = 16$), respectively (Extended Data Table 3). Hence, the water abundance of the bulk CE6 basalt is $1.1 \pm 0.5 \mu\text{g g}^{-1}$ (1 s.d.). Apatite is a late-crystallizing mineral in mare basalts; its notably higher δD values ($826 \pm 94\%$) than the low- δD ($-200 \pm 200\%$) nature of lunar mantle^{9,23,40,62} and low δD of CE6 melt inclusions indicate strong degassing and loss of water in the form of H_2 (refs. 24,25). The hydrogen isotope fractionation during volatile loss into a vacuum is given by $\alpha^2 = M_1/M_2$, where M_1 and M_2 are the masses of the volatile phase isotopologues. The change of the isotopic composition of H during volatile loss by Rayleigh fractionation is given by $R = R_0 \times f^{(\alpha-1)}$, where R_0 and R are the initial and final D/H ratios for a fraction of remaining hydrogen. Degassing of H_2 ($M_1 = 2$ for H_2 and $M_2 = 3$ for HD) yields an α value of about 0.8165 (ref. 25). Degassing modelling indicates that the crystallization of apatite grains in CE6 mare basalt started at the time when 97.99–99.35% of initial water in the parent melt has been degassed. After degassing loss correction, the water abundance of the parent melt is about $55 \pm 25 \mu\text{g g}^{-1}$ to $168 \pm 77 \mu\text{g g}^{-1}$ (1 s.d.).

In another viable approach^{1,26,27}, the authors have developed apatite-based melt hygrometry methodologies, to estimate parent magma water abundance using apatite. These methods are designed to estimate parent melt water abundances from apatite regardless of how much H-degassing has occurred after apatite crystallization. The measured F and H_2O abundance in apatite from each fragment was used to derive the parental melt H_2O , using a 0.07 vol% modal abundance of apatite (Supplementary Table 2). The results yield H_2O abundance of 59–99 $\mu\text{g g}^{-1}$ for the parental magma (Supplementary Table 6), plotting within the approximately 55–168 $\mu\text{g g}^{-1}$ range of the other method presented earlier. Considering the early entrapment of olivine-hosted melt inclusions¹⁷, these targets were used to estimate the water abundance for the mantle source.

Data availability

All geochemical data generated in this study are included in Extended Data Tables 1–3 and Supplementary Tables 1–7 and are available at Zenodo⁶⁴ (<https://doi.org/10.5281/zenodo.14916067>).

46. Ji, J. et al. Improved Pb-Free Sn-Bi alloy mounting technique for ion probe U-Pb analyses of zircon. *At. Spectrosc.* **43**, 207–213 (2022).
47. Li, Q.-L. et al. Two-billion-year-old volcanism on the Moon from Chang'e-5 basalts. *Nature* **600**, 54–58 (2021).
48. Tian, H. C. et al. Non-KREEP origin for Chang'e-5 basalts in the Procellarum KREEP Terrane. *Nature* **600**, 59–63 (2021).
49. Barnes, J. J. et al. Accurate and precise measurements of the D/H ratio and hydroxyl content in lunar apatites using NanoSIMS. *Chem. Geol.* **337–338**, 48–55 (2013).

50. McCubbin, F. M. et al. Detection of structurally bound hydroxyl in fluorapatite from Apollo Mare basalt 15058,128 using TOF-SIMS. *Am. Mineral.* **95**, 1141–1150 (2010).
51. Hauri, E. et al. SIMS analysis of volatiles in silicate glasses: 1. Calibration, matrix effects and comparisons with FTIR. *Chem. Geol.* **183**, 99–114 (2002).
52. Hu, S. et al. Measurements of water content and D/H ratio in apatite and silicate glasses using a NanoSIMS 50L. *J. Anal. At. Spectrom.* **30**, 967–978 (2015).
53. Li, R. Y. et al. High-spatial-resolution measurement of water content in Olivine using NanoSIMS 50L. *At. Spectrosc.* **43**, 77–83 (2022).
54. Hu, S. et al. NanoSIMS analyses of apatite and melt inclusions in the GRV 020090 Martian meteorite: Hydrogen isotope evidence for recent past underground hydrothermal activity on Mars. *Geochim. Cosmochim. Acta* **140**, 321–333 (2014).
55. Greenwood, J. P., Itoh, S., Sakamoto, N., Vicenzi, E. P. & Yurimoto, H. Hydrogen isotope evidence for loss of water from Mars through time. *Geophys. Res. Lett.* **35**, L05203 (2008).
56. Nadeau, S. L., Epstein, S. & Stolper, E. Hydrogen and carbon abundances and isotopic ratios in apatite from alkaline intrusive complexes, with a focus on carbonatites. *Geochim. Cosmochim. Acta* **63**, 1837–1851 (1999).
57. Hoefs, J. *Stable Isotope Geochemistry* (Springer, 2009).
58. Zhang, W. F. et al. Optimization of SIMS analytical parameters for water content measurement of olivine. *Surf. Interface Anal.* **52**, 224–233 (2019).
59. Tartese, R., Anand, M. & Franchi, I. A. H and Cl isotope characteristics of indigenous and late hydrothermal fluids on the differentiated asteroidal parent body of Grise Nunataks 06128. *Geochim. Cosmochim. Acta* **266**, 529–543 (2019).
60. Füri, E., Delouze, E. & Trappitsch, R. The production rate of cosmogenic deuterium at the Moon's surface. *Earth Planet. Sci. Lett.* **474**, 76–82 (2017).
61. Merlini, L., Leiu, M., Neif, G. & Roth, E. Spallation deuterium in rock 70215. In *Proc. Lunar Science Conference Vol. 1*, 649–658 (Pergamon Press, 1976).
62. Tartese, R. et al. Apatites in lunar KREEP basalts: The missing link to understanding the H isotope systematics of the Moon. *Geology* **42**, 363–366 (2014).
63. Wu, F.-Y. et al. Lunar evolution in light of the Chang'e-5 returned samples. *Annu. Rev. Earth Planet. Sci.* **52**, 159–194 (2024).
64. Hu, S. Supplementary data tables to "Water abundance in the lunar farside mantle". *Zenodo* <https://doi.org/10.5281/zenodo.14916067> (2025).
65. Ni, P., Zhang, Y. X. & Guan, Y. B. Volatile loss during homogenization of lunar melt inclusions. *Earth Planet. Sci. Lett.* **478**, 214–224 (2017).
66. Wetzel, D. T., Hauri, E. H., Saal, A. E. & Rutherford, M. J. Carbon content and degassing history of the lunar volcanic glasses. *Nat. Geosci.* **8**, 755–758 (2015).

Acknowledgements We thank F. M. McCubbin and another anonymous referee for their comments and suggestions for improving the quality of the paper; D. Chew for providing Durango and Kovdor apatite; E. Hauri for providing basaltic glass 519-4-1 and 1833-11 and anhydrous Suprasil 3001; R. Francis for providing SWIFT MORB glass; R. Mitchell, X.-H. Li and F.-Y. Wu for their comments and editing; S. Gou for map drafting; Y. Chen and L. Jia for assistance with EPMA measurement; W. Yang, H. Tian and H. Ma for hand-picking the CE6 soil fragments; and L. Gu and X. Tang for assistance with scanning electron microscopy observation. This study was funded by the National Natural Science Foundation of China (42125303 and 42241104), the Strategic Priority Research Program of Chinese Academy of Sciences (XDB 41000000), the China National Postdoctoral Program for Innovative Talents (BX20240365), and the key research programme of the Institute of Geology and Geophysics, Chinese Academy of Sciences (IGGCAS-202401 and 202204). The CE6 samples were allocated by the China National Space Administration (CNSA).

Author contributions S.H., Y.L. and H. Hui designed this research. H. He., L.L., Y.G., L.G., Z.Z., M.Q., D.Z., R.L., H.L. and S.H. prepared the sample and characterized the petrography and mineral chemistry of CE6 basalts. H. He., Y.G., L.L., R.L., J.H. and S.H. conducted the NanoSIMS measurements. S.H., Y.L., H. Hui, H. He, L.L. and Y.G. wrote the paper. All authors contributed to the preparation of the paper.

Competing interests The authors declare no competing interests.

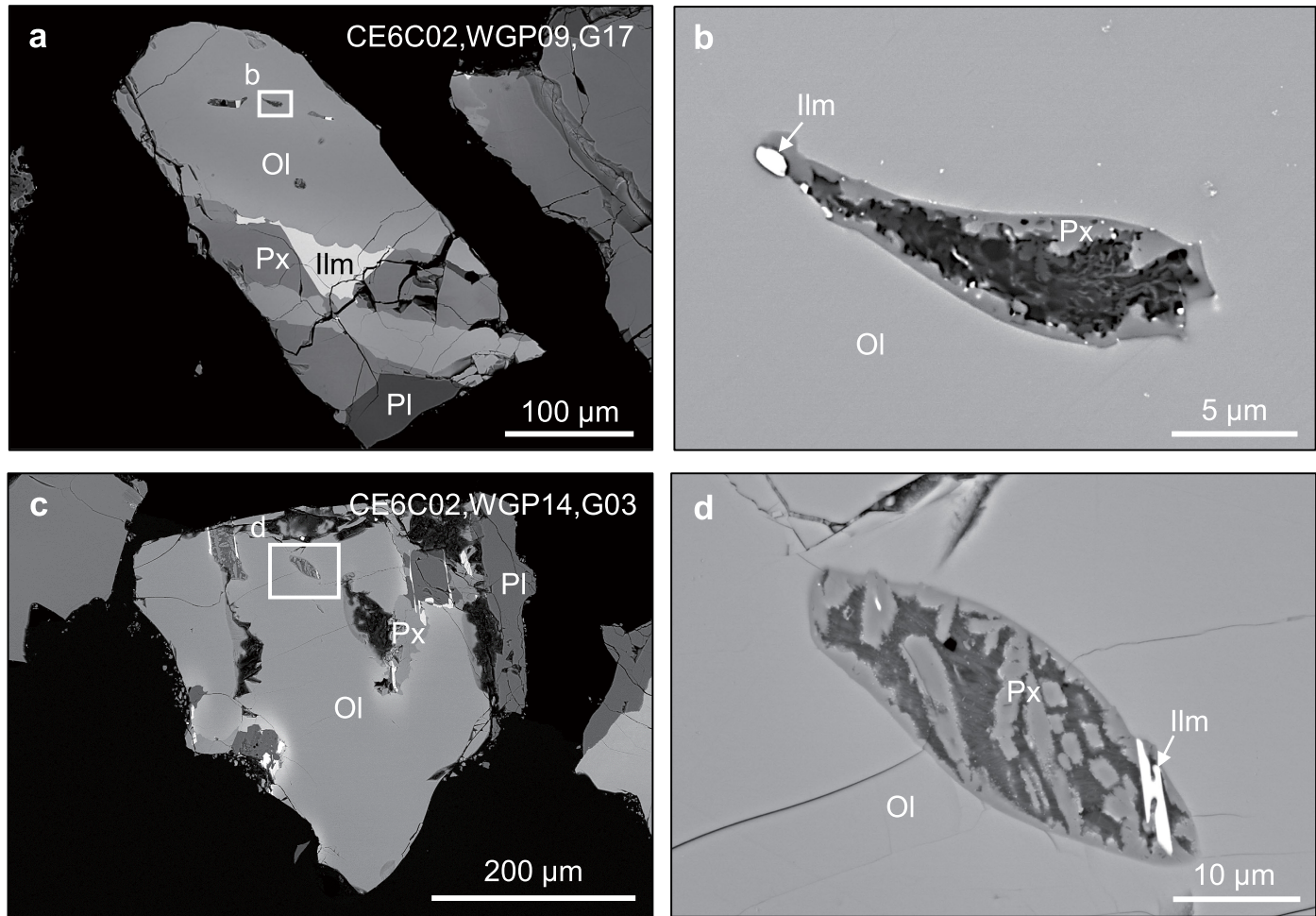
Additional information

Supplementary information The online version contains supplementary material available at <https://doi.org/10.1038/s41586-025-08870-x>.

Correspondence and requests for materials should be addressed to Sen Hu, Hejiu Hui or Yangting Lin.

Peer review information *Nature* thanks Francis McCubbin and the other, anonymous, reviewer(s) for their contribution to the peer review of this work. Peer reviewer reports are available.

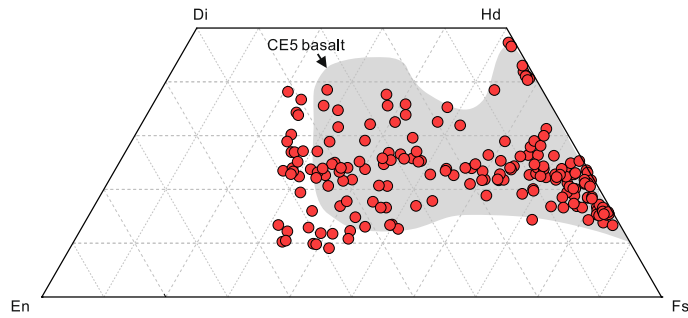
Reprints and permissions information is available at <http://www.nature.com/reprints>.



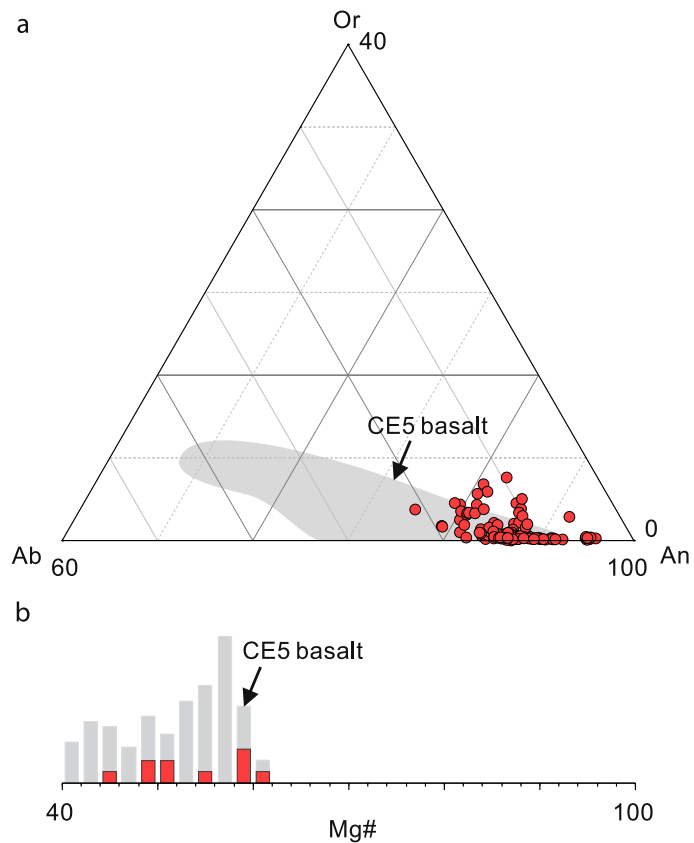
Extended Data Fig. 1 | Petrography of olivine-hosted melt inclusions identified in CE6 mare basalt fragments. Olivine is quite rare in CE6 mare basalt. Only two in total of 163 CE6 mare basalt fragments surveyed were found to contain olivine hosting melt inclusions. These melt inclusions exhibit post-entrapment crystallisation as indicated by the presence of pyroxene and

ilmenite. The host olivine is MgO-rich with forsterite (Fo) content of 45.0–61.6 atom% (Supplementary Data Table 3). The NanoSIMS analytical positions are labeled in Supplementary Fig. 1. OI, olivine; Px, pyroxene; PI, plagioclase; ILM, ilmenite.

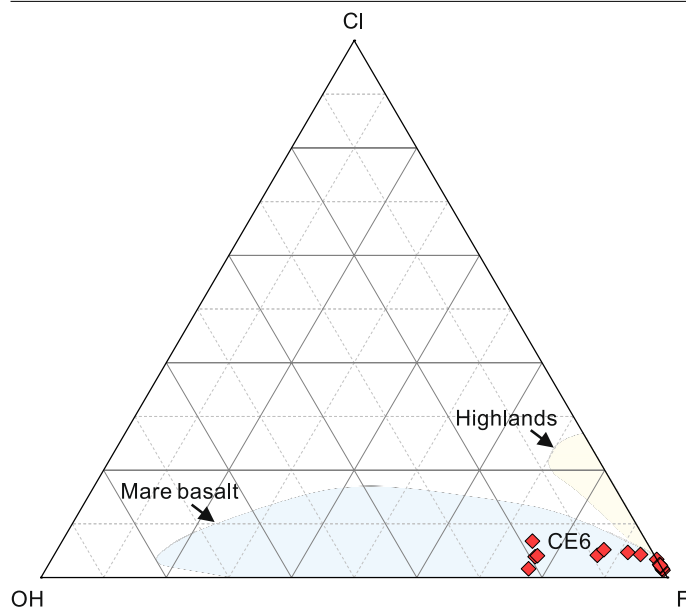
Article



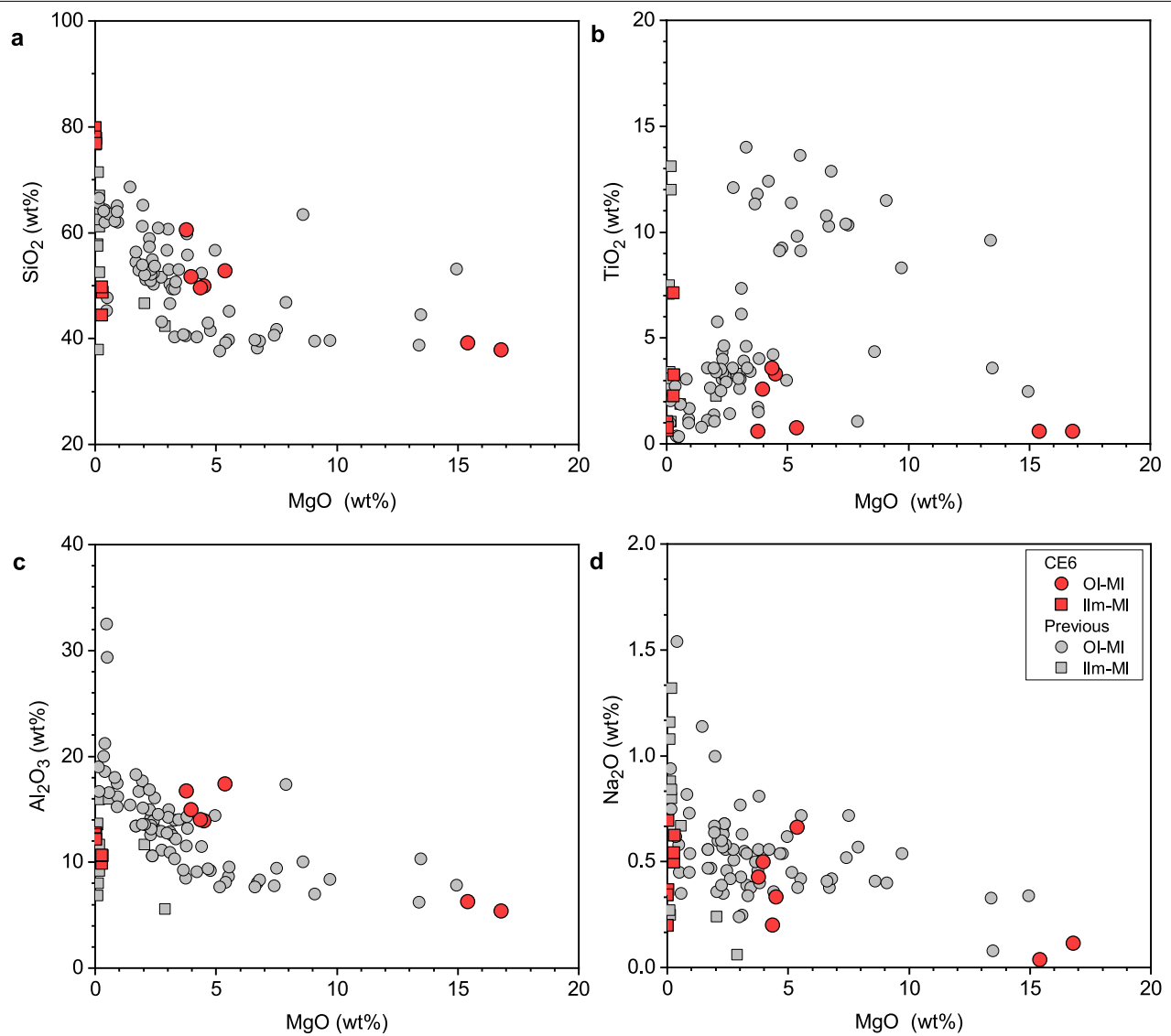
Extended Data Fig. 2 | Pyroxene quadrilateral diagram of the CE6 mare basalt fragments. The CE6 mare basalt fragments (red) are plotted in the same range of CE5 (gray field), with relative lower FeO contents⁶³. All data are listed in Supplementary Data Table 3. Di, diopside; En, enstatite; Fs, ferrosilite; Hd, hedenbergite.



Extended Data Fig. 3 | Major-element compositions of plagioclase and olivine in CE6 mare basalt fragments. **a**, Ternary diagram of plagioclase. **b**, Histogram exhibiting variation of Mg number (Mg#, Mg/(Mg+Fe) atom%) of olivine. Or, orthoclase; Ab, albite; An, anorthite. All data are listed in Supplementary Data Table 3. CE6 data are in red. Data of CE5 mare basalt (gray) are shown for comparison⁶³.

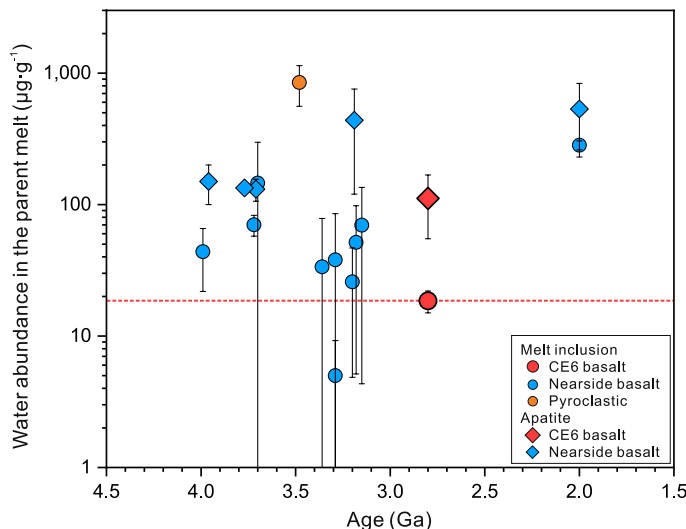


Extended Data Fig. 4 | The ternary atomic plot of apatite from CE6 basalt clasts. Concentrations of Cl and F were measured using EPMA, and OH was calculated based on the stoichiometry of apatite. Fields for apatite compositions from mare basalts and highlands refer to previous work¹. CE6 data are in red and are listed in Supplementary Data Table 3.

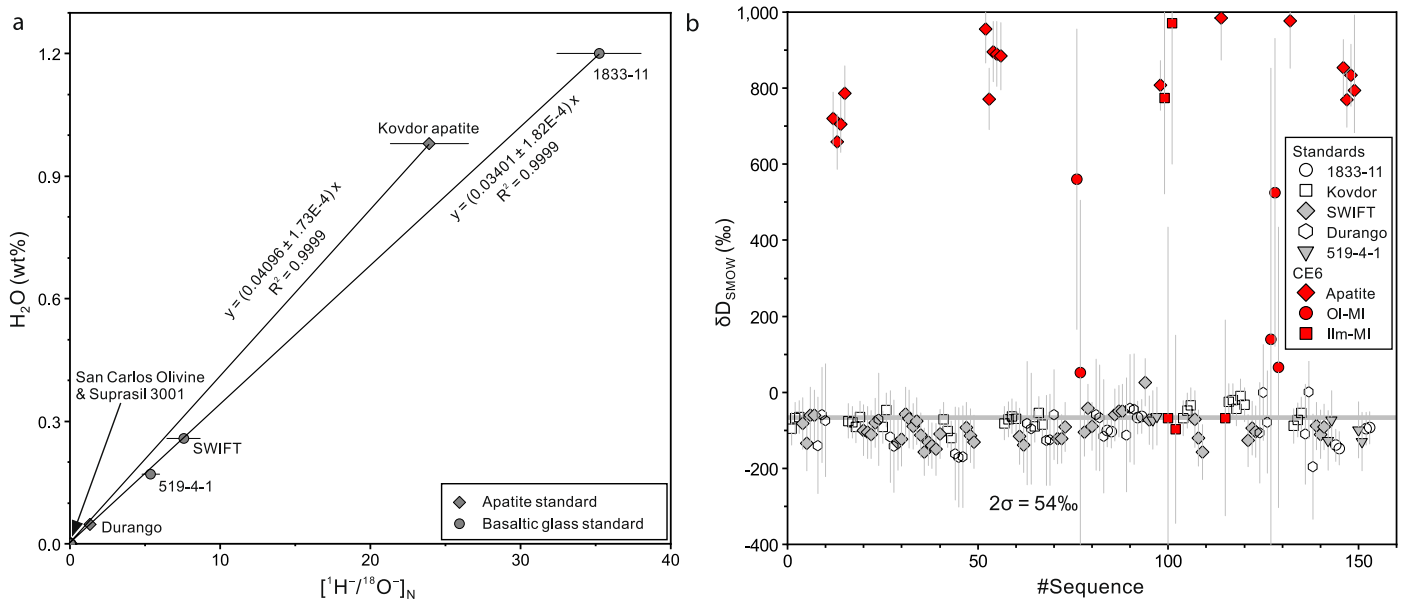


Extended Data Fig. 5 | Major-element compositions of melt inclusions in CE6 mare basalt fragments. Variations of SiO_2 (a), TiO_2 (b), Al_2O_3 (c), and Na_2O (d) contents with MgO contents in olivine- (OI-MI) and ilmenite-hosted (IIm-MI)

melt inclusions. Previous data from refs. 23,30,32 are plotted for comparation. OI-MI have notably higher MgO contents than IIm-MI, suggesting earlier entrapment for the former. All data are listed in Supplementary Data Table 3.



Extended Data Fig. 6 | Parent melt water abundances of CE6 mare basalt compared with estimates from nearside samples. Very low-Ti pyroclastic glass 15427 from ref. 14; low-Ti mare basalt 12002, 12004, 12008, 12020, 12040, 15016, 12039, 12064, 15555, and 15058 from ref. 23; high-Ti mare basalt Apollo 10020, 10044, 74235, and 75055 from refs. 23, 30, 32; high-Ti pyroclastic melt inclusions in 74220 from refs. 17, 30, 32, 42, 65, 66; high-Al basalt 14072 and 14053 from refs. 15, 23. The error bars represent the ranges of the parent melt water abundances estimated from lunar samples in the literature. The red dashed line is a reference at $18.5 \mu\text{g}\cdot\text{g}^{-1}$ for comparison.



Extended Data Fig. 7 | Water content calibration line and reproducibility of hydrogen isotope analysis established on apatite and silicate glass standards. **a**, A water calibration curve was established using the following standards: two apatite (Kovdor and Durango), three basaltic glasses (ALV-1833-11, ALV-519-4-1, and SWIFT MORB glass), and two anhydrous background (San Carlos olivine and Suprasil 3001). The datasets are listed in Supplementary Data Table 4. The analytical uncertainties are 0.42 % and 0.54 % (1σ) for apatite and glasses, respectively. **b**, Reproducibility of the hydrogen isotope analysis of the standards and the CE6 apatite and melt inclusions over the analytical

session. The reproducibility of δD analysis throughout the whole analytical sessions was $\pm 54\text{‰}$ (2σ), estimated on the Kovdor apatite standard. The average δD values measured for the SWIFT MORB glass and Durango apatite are $-98 \pm 70\text{‰}$ and $-97 \pm 100\text{‰}$, respectively, consistent with their recommended values (-73‰ and -120‰)^{16,55} within analytical errors. The average δD values measured for the basaltic glass standards ALV-1833-11 and ALV-519-4-1 are $-101 \pm 60\text{‰}$ and $-94 \pm 58\text{‰}$, consistent with previous measured values of $-101 \pm 86\text{‰}$ and $-132 \pm 158\text{‰}$, in ref. 9. Data are listed in Extended Data Tables 2, 3 and Supplementary Data Tables 4, 5.

Article

Extended Data Table 1 | Mount information summary of 21 mounts in this study

#Seq	Mount#	Grain size	Agglutinate	Basalt	Breccia	Glass fragment	Highlands	Impact melt	Monomineral	Sum
1	CE6C02,MGP01	>355µm		2	1	2	2	1		8
2	CE6C02,MGP02	>355µm		3	4	1		2		10
3	CE6C02,MGP03	>355µm			4		4	3		11
4	CE6C02,MGP04	>355µm		1	3			2		6
5	CE6C02,MGP05	>355µm	1	2	10	1	2	1	1	18
6	CE6C02,MGP06	>355µm	3	6	3	2		6		20
7	CE6C02,MGP07	>355µm	2	5	7				1	15
8	CE6C02,WGP01	<355µm	5	1		5		2	9	22
9	CE6C02,WGP02	<355µm	4	1	4	1	4	1	3	18
10	CE6C02,WGP03	<355µm	3	4	2	2	1	4	1	17
11	CE6C02,WGP04	<355µm	1	9	3			3	6	22
12	CE6C02,WGP05	<355µm	4	8		3	2	7	2	26
13	CE6C02,WGP06	<355µm	2	9	2	2	2		5	24
14	CE6C02,WGP07	<355µm	3	11	7	1	2		1	25
15	CE6C02,WGP08	<355µm	2	11		3	1	3	7	27
16	CE6C02,WGP09	<355µm	1	21	11	5	6	3	18	65
17	CE6C02,WGP10	<355µm	6	18	9	5	5	12	5	60
18	CE6C02,WGP11	<355µm	6	12	5	4	12	9	14	62
19	CE6C02,WGP12	<355µm		20	9		9	8	14	60
20	CE6C02,WGP13	<355µm	3	6	9	1		6	6	31
21	CE6C02,WGP14	<355µm	4	14	8	1			4	31
Sum				50	164	101	39	52	75	97
Fraction (%)				8.7	28.4	17.5	6.7	9.0	13.0	16.8

f is fraction given as a percentage.

Extended Data Table 2 | Water abundance and hydrogen isotopes of melt inclusions in CE6 basalts

Sample information			Background and IMF corrected value				CRE-corrected value				PEC-corrected value				
Filename	Mount#	Grain#	H ₂ O μg·g ⁻¹	2σ μg·g ⁻¹	δD ‰	2σ ‰	H ₂ O μg·g ⁻¹	2σ μg·g ⁻¹	δD ‰	2σ ‰	PEC %	H ₂ O μg·g ⁻¹	2σ μg·g ⁻¹	δD ‰	2σ ‰
<i>Olivine-hosted MI</i>															
HD0829-WGP09-G17_4	CE6C02,WGP09	G17	14	5	1099	535									
HD0829-WGP09-G17_5	CE6C02,WGP09	G17	14	6	2252	501									
HD0829-WGP09-G17_7	CE6C02,WGP09	G17	28	8	560	448	28	8	93	515	31	19	5	93	515
HD0829-WGP09-G17_9	CE6C02,WGP09	G17	32	9	53	570	32	9	-358	610	43	18	5	-358	610
HD0831-WGP14-G03_2	CE6C02,WGP14	G03	12	1	139	968									
HD0831-WGP14-G03_3	CE6C02,WGP14	G03	31	2	526	414	30	2	100	474	52	15	1	100	474
HD0831-WGP14-G03_4	CE6C02,WGP14	G03	46	2	65	395	46	2	-221	423	52	22	1	-221	423
avg.					34				-96			19			-96
1SD					8				230			3			230
<i>Ilmenite-hosted MI</i>															
HD0829-WGP10-G53_3	CE6C02,WGP10	G53	184	3	-68	515	184	3	-140	517	n.	184	3	-140	517
HD0830-WGP12-G57_2	CE6C02,WGP12	G57	154	4	-97	257	153	4	-183	261	n.	153	4	-183	261
HD0830-MGP02-G09_3	CE6C02,MGP02	G09	159	4	-68	268	159	4	-151	271	31	110	3	-151	271
Early trapped melt															
avg.							165		-158			149			-158
1SD							16		23			37			23
δD for mantle															
1SD									-123			167			
HD0828-WGP06-G20_1	CE6C02,WGP06	G20	21	3	2352	469	21	3	1762	588	29	15	2	1762	588
HD0828-WGP06-G20_2	CE6C02,WGP06	G20	23	3	1063	622	22	3	488	700	29	16	2	488	700
HD0829-WGP10-G53_2	CE6C02,WGP10	G53	238	21	773	252	238	21	719	254	n.	238	21	719	254
HD0829-WGP10-G17_2	CE6C02,WGP10	G17	233	5	970	373	232	5	915	374	28	167	3	915	374
HD0830-WGP12-G32_1	CE6C02,WGP12	G32	141	2	1099	202	141	2	1008	208	n.	141	2	1008	208
HD0830-WGP08-G12_2	CE6C02,WGP08	G12	23	2	1891	487	23	2	1344	584	n.	23	2	1344	584
HD0830-WGP08-G12_3	CE6C02,WGP08	G12	17	2	1576	540									
HD0830-WGP08-G12_4	CE6C02,WGP08	G12	8	1	4121	560									
HD0830-WGP08-G12_5	CE6C02,WGP08	G12	11	1	1354	699									
Late trapped melt															

A cosmic ray exposure (CRE) age of 108 Ma was used for correction of spallation effects (Methods). The spots with water abundance less than 20 μg·g⁻¹ are not listed δD values.
n. No post-entrainment crystallisation (PEC) correction.

Article

Extended Data Table 3 | Water abundance and hydrogen isotopes of apatite grains in CE6 basalts

Sample information			Background and IMF corrected value				CRE-corrected value			
Filename	Mount#	Grain#	H ₂ O	2σ	δD	2σ	H ₂ O	2σ	δD	2σ
			μg·g ⁻¹	μg·g ⁻¹	‰	‰	μg·g ⁻¹	μg·g ⁻¹	‰	‰
HD0826-WGP05-G06_2	CE6C02,WGP05	G06	2055	24	720	70	2055	24	718	70
HD0826-WGP05-G06_3	CE6C02,WGP05	G06	2032	24	659	72	2031	24	657	72
HD0826-WGP05-G06_4	CE6C02,WGP05	G06	1864	23	705	74	1864	23	702	74
HD0826-WGP05-G20_1	CE6C02,WGP05	G20	1541	21	786	73	1540	21	782	73
HD0828-WGP06-G20_6	CE6C02,WGP06	G20	977	10	956	87	977	10	951	87
HD0828-WGP06-G19_1	CE6C02,WGP06	G19	1403	14	772	80	1403	14	768	80
HD0828-WGP06-G19_2	CE6C02,WGP06	G19	1320	14	896	78	1319	14	892	78
HD0828-WGP06-G19_3	CE6C02,WGP06	G19	1030	15	890	84	1030	15	885	84
HD0828-WGP06-G19_6	CE6C02,WGP06	G19	982	14	884	87	981	14	879	87
HD0830-WGP12-G56_1	CE6C02,WGP12	G56	3530	30	807	65	3529	30	806	65
HD0830-WGP09-G28_1	CE6C02,WGP09	G28	506	7	984	109	506	7	974	109
HD0831-WGP14-G06_2	CE6C02,WGP14	G06	346	4	977	123	345	4	963	123
HD0831-MGP06-G05_1	CE6C02,MGP06	G05	1662	14	854	75	1662	14	851	75
HD0831-MGP06-G05_2	CE6C02,MGP06	G05	2087	18	769	72	2087	18	767	72
HD0831-MGP06-G18_1	CE6C02,MGP06	G18	1278	12	834	82	1277	12	830	82
HD0831-MGP06-G18_2	CE6C02,MGP06	G18	1577	43	794	199	1577	43	791	199
avg.			1512		830		1511		826	
1SD			748		97		748		94	

A cosmic ray exposure (CRE) age of 108 Ma was used for correction of spallation effects (Methods).